Analysis and Stabilization of APF Systems Considering Dynamic of Nonlinear Loads

Yuguo Li, *Student Member, IEEE*, Hao Yi, *Member, IEEE*, Fang Zhuo, *Member, IEEE*, and Xin Jiang, *Graduate Student Member, IEEE*

***Abstract*—The active power filter (APF) is effective for harmonic suppression. But it may cause harmonic oscillation under certain source-load conditions. This article analyzes the harmonic oscillation and its stabilization. The dynamics of the APF's current control and the nonlinear load's frequency coupling effect are considered, which are normally ignored in existing research. It is found that the frequency coupling effect makes symmetric harmonics (−5th/7th, −11th/13th, for example) share their harmonic dynamics and oscillate or converge together. And the APF's current controller can provide harmonic damping. Then two regular harmonic stabilizing methods, harmonic suppressing ratio reducing (SRR) and harmonic virtual admittance (HVA) control, are reassessed considering the nonlinear load. Analyzing results show that frequency coupling caused by the nonlinear load has different impacts on the SRR and HVA, which provides theoretical guidance for choosing or designing stabilizing strategies. Models in this article are verified by frequency-sweeping simulation, and analyzing conclusions about the oscillation features and stabilizing methods are verified by both simulations and experiments.**

***Index Terms*—Active power filter (APF), harmonic resonance instability, nonlinear load dynamic modeling, stabilizing methods.**

Nomenclature

$\Delta(s)$	Characteristic polynomial of the APF system.
ω_1	Frequency of the ac-bus (grid).
φ_{rk}	Phase adjustment of the APF's kth harmonic resonance controller.
$D(s), D_k(s)$	Transfer function of the whole harmonic detecting algorithm and kth harmonic detecting algorithm.
$G_i(s)$	Closed-loop dynamic response characteristic.
$H_i(s)$	Transfer function of the current controller.
I_{ck}, I_{Lk}	Phasor of steady-state kth harmonic component of APF's output current and nonlinear load's input current.
K_p	Proportional gain of the APF's current controller.
K_{rk}	Gain of the APF's kth harmonic current resonance controller.
L, R, C	Parameters of the grid-side impedance.
$T(s)$	Equivalent loop gain of the APF system.
$T_p(s)$	Sequence loop gain of the APF system.
$Y(s)$	Input admittance of the APF.
$Z_g(s)$	Grid-side impedance.

Manuscript received 19 February 2023; revised 22 August 2023; accepted 3 October 2023. Date of publication 16 October 2023; date of current version 6 December 2023. This work was supported by the National Natural Science Foundation of China under Grant 51977172. Recommended for publication by Associate Editor H. L. Ginn. *(Corresponding author: Hao Yi.)*

The authors are with the State Key Laboratory of Electrical Insulation and Power Equipment, School of Electrical Engineering, Xi'an Jiaotong University, Xi'an 710049, China (e-mail: rascal@stu.xjtu.edu.cn; yi_hao@mail.xjtu.edu.cn; zffz@mail.xjtu.edu.cn; 3120104229@stu.xjtu.edu.cn).

Color versions of one or more figures in this article are available at https://doi.org/10.1109/TPEL.2023.3324650.

Digital Object Identifier 10.1109/TPEL.2023.3324650

I. Introduction

THE active power filter (APF) is an effective and flexible device to deal with the harmonic issue introduced by nonlinear loads [1] and improve the power quality. Till now, designing of APFs has been researched in detail, including algorithms of harmonic detection [2], [6], [7], [8], [9], current control methods [3], [4], [5], and topology improvement [10]. However, utilization of the APF leads to a potential resonance characteristic that interacts with nonlinear loads and the system impedance to form a parasitic feedback system called "APF system." The dynamic interaction sometimes activates the potential resonance to trigger an issue of stability, damaging the effectiveness of the APF.

Recent research works suggest that the stability issue includes two categories: high-frequency resonance and harmonic oscillation. Literature [11], [12], [13], [14], and [15] researched the high-frequency resonance of an APF system. Their results show that high-frequency resonance is mainly determined by the current-inner-loop parameters, digital control delay, and system passive resonance frequency, which is similar to high-frequency resonance of voltage source grid-connected converters (VSCs). So, high-frequency resonance issue of the APF can be dealt with by regular active damping strategies, such as digital control delay compensation [15], [16], [17], auxiliary current feedback [18], [19], or voltage feedback [15].

The other stability issue, harmonic oscillation, typically occurs around the harmonics under suppression. The grid-side impedance, APF's current inner loop (CIC), the dynamic of nonlinear loads, and harmonic detection methods all impact it. Therefore, the harmonic oscillation issue is more challenging than the high-frequency resonance. Harmonic oscillation has not been covered in great detail, though. In [20] and [21], it was examined how the power factor correcting (PFC) capacitors paralleled with the nonlinear load affected the harmonic

instability of the APF system. It was discovered that the harmonic oscillation propensity of the APF system was activated by the resonance interaction between the grid-side impedance and the PFC capacitors.

However, the conclusions in [20] and [21] are overly conservative for two reasons. First, the nonlinear load is viewed as a straightforward Norton equivalent circuit, whereas the system can be dampened by the frequency coupling effect that the nonlinearity introduces. Second, dynamic of the APF's CIC also has a damping effect that enhances stability, whereas the dynamic is ignored in [20] and [21]. Although CIC was taken into account in [22] and [23], the harmonic controller group (resonance or repetitive controllers), which is crucial for the harmonic stability of the APF system, was not.

To further investigate the harmonic oscillation issue and draw more accurate conclusions, the harmonic current controller group (composed of resonance controllers in this article) and nonlinear load are taken into account in this study. The nonlinear load is found to have a frequency coupling effect and is modeled through harmonic linearization [24], [25]. Then grid-side impedance, the APF, and the 6-pulse rectifier are considered as a whole to analyze the harmonic oscillation issue. Findings indicate that both the frequency coupling and harmonic current controller have a sizable impact on the harmonic stability of the APF system.

Two stabilizing methods, suppressing ratio reduction (SRR) and harmonic virtual admittance (HVA), are then evaluated to demonstrate once more how important it is to consider the nonlinear load's frequency coupling effect. Conclusions help select and design effective harmonic stabilization with appropriate harmonic suppressing precision lost.

The rest of this article is organized as follows. Section II introduces the APF parasitic feedback system and explains concepts of the parasitic system and the harmonic oscillation issue qualitatively. Section III gives out the modeling process of the APF and the 6-pulse rectifier. Here, how 6-pulse rectifier causes frequency coupling is explained. Section IV describes how harmonic oscillation occurs under the impact of key factors. Section V assessed the two stabilizing methods (SRR & HVA), revealing how frequency coupling affects their effectiveness. Section VI gives out simulation and experimental results to verify the conclusions. Finally, Section VII concludes this article.

II. Qualitative Interpretation of the APF's Harmonic Resonance Phenomenon

The APF system examined in this article is shown in Fig. 1. A 6-pulse diode rectifier with an *RLC* load is chosen as the nonlinear load. The grid-side impedance $Z_g(s)$ includes line inductor L, line resistor R, and PFC capacitor C. The APF works in load-current-detected mode. Indicated harmonics in the load current are detected through the harmonic current detecting (HCD) algorithm as i_{ref}, and current inner-loop control (CIC) makes sure the APF's output current i_c adheres to i_{ref}.

Due to $Z_g(s)$, a parasitic dynamic feedback loop of $i_g \rightarrow v_g \rightarrow i_g$ is formed, which interconnects the APF, rectifier, and

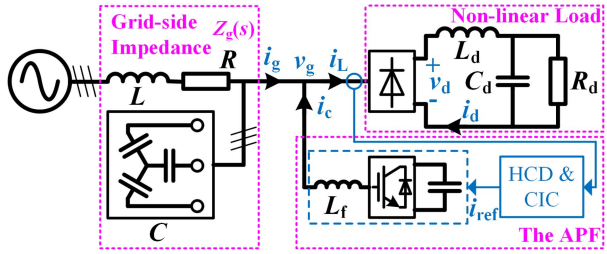

Fig. 1. Structure of the APF system.

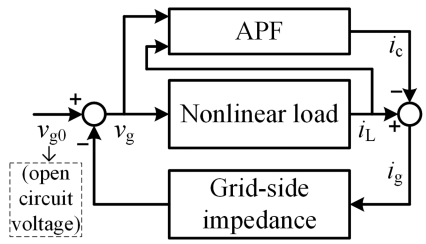

Fig. 2. Parasitic feedback relationship within the APF system.

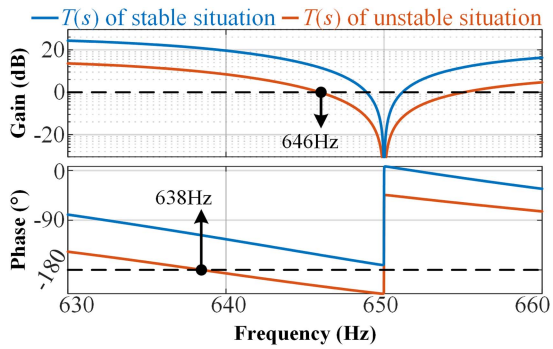

Fig. 3. Bode plots of the equivalent loop gain $T(s)$ around 13th harmonic resonance valley.

$Z_g(s)$ together and results in a parasitic feedback system (the APF system), as shown in Fig. 2.

The parasitic system introduces unanticipated dynamics and causes different types of dynamic issues. In the APF system, APF maintains indicated suppressed harmonics in i_g at an ignorable level, even if v_g has these harmonic components. So the parallel admittance of the APF and nonlinear load is very small around the harmonics, which means parallel resonance and gives the APF system a propensity to oscillate.

Equivalent loop gain $T(s)$ (will be derived in Section IV) is shown here to explain the oscillating propensity. Fig. 3 shows bode plots of $T(s)$ around the 13th harmonic ($13\omega_1$), corresponding to the stable and unstable situations. The APF's suppression on the 13th harmonic causes a resonance valley (corresponding to the aforementioned parallel resonance) at $13\omega_1$, where $\angle T(s)$ has a sharp step. This sharp step makes $\angle T(s)$ possible to cross $\pm 180°$ under the phase deviating effect of other factors in the system.

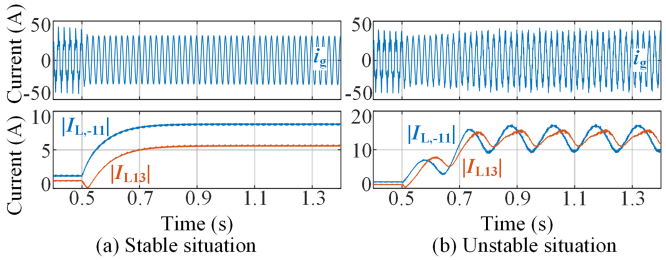

Fig. 4. Bode plots of the equivalent loop gain $T(s)$ around 13th harmonic resonance valley.

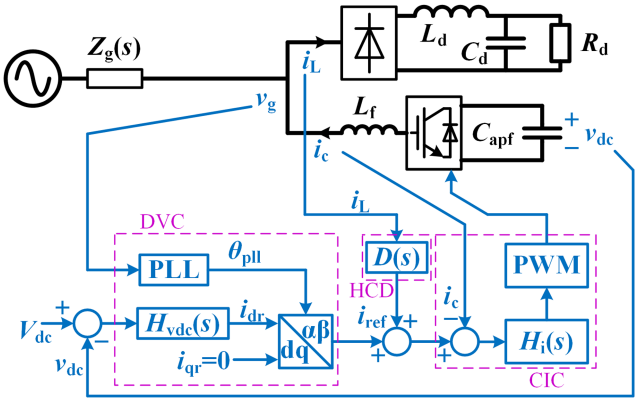

Fig. 5. Block diagram of the APF control system.

As shown in the corresponding simulation waveforms in Fig. 4, in an unstable situation, $|I_{L13}|$ (amplitude of the 13th harmonic in load current i_L) oscillates at a low frequency and is higher than that of a stable situation, which means that the harmonic oscillation is harmful to power quality.

Equivalent loop gain $T(s)$ is influenced by all of the key components in the APF system ($Z_g(s)$, nonlinear load, HCD, and CIC), as shown in Fig. 1, whereas the two situations in Figs. 3 and 4 are different only in $Z_g(s)$. So, more investigation is necessary.

More importantly, both $|I_{L13}|$ and $|I_{L,-11}|$ oscillate in Fig. 4, which usually happens in reality. This article finds that this phenomenon is caused by the frequency coupling effect of the nonlinear load, which is ignored in existing literature, so the frequency coupling is emphasized in this article. Following sections model the key components and do quantitative analysis.

III. Modeling of the APF and Nonlinear Load

A. Modeling of the APF

This article focuses on stability assessment. Thus, small-signal linear models [30], [31] are derived. The control system of the APF is shown in Fig. 5. Apparently, the APF control system has two inputs (load current i_L and ac bus voltage v_g), and one output (APF compensating current i_c). So the small-signal model of APF is in the form of (1). $A(s)$ is the dynamic response from i_L to i_c and $Y(s)$ is that of APF's input admittance

$$\hat{i}_c(s) = A(s)\hat{i}_L(s) - Y(s)\hat{v}_g(s). \tag{1}$$

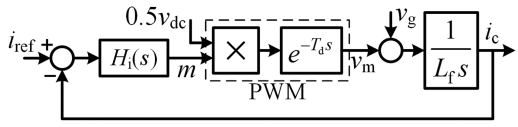

Fig. 6. Structure of the current inner-loop control (CIC).

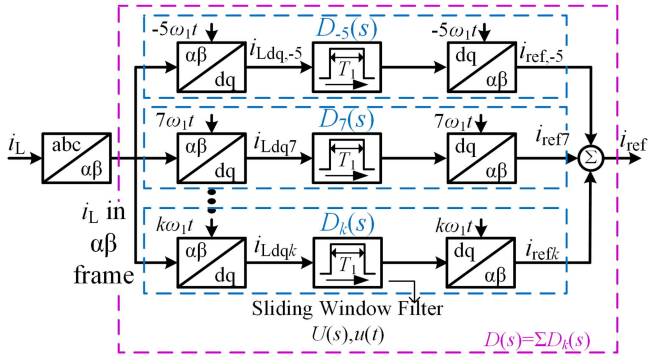

Fig. 7. Structure of the current inner-loop control (CIC).

As shown in Fig. 5, the control system of APF is composed of three major parts that are current inner-loop control (CIC), harmonic current detection (HCD), and dc voltage control (DVC). The following part considers them, respectively, to derive $A(s)$ and $Y(s)$ in (1).

Fig. 6 shows the structure of CIC. CIC has three inputs (i_{ref}, v_{dc}, and v_g) and one output (i_c). Current reference i_{ref} is the sum of HCD's and DVC's output. It is easy to derive the model of CIC as (2). $H_i(s)$ refers to the current proportional-resonance controller [as shown in (3)], and $R_k(s)$ denotes the resonance controllers. T_d refers to the digital control delay. The phasor M_1 is the steady-state component of the PWM modulation wave m. In the variables and subscripts, k denotes harmonic order in this article

$$\hat{i}_c = G_i(s)\hat{i}_{ref} - Y(s)\hat{v}_g + 0.5M_1Y(s)e^{-T_d s}\mathrm{L}\left\{e^{j\omega_1 t}\hat{v}_{dc}\right\}$$

$$G_i(s) = \frac{H_i(s)e^{-T_d s}}{L_f s + H_i(s)e^{-T_d s}}, Y(s) = \frac{1}{L_f s + H_i(s)e^{-T_d s}} \tag{2}$$

$$H_i(s) = K_p + \sum_k \underbrace{\frac{K_{rk}e^{j\varphi_{rk}}}{s - jk\omega_1}}_{R_k(s)}. \tag{3}$$

In the view of the frequency domain, HCD operates as a bandpass filter that extracts specified harmonics in load current i_L. So various HCD strategies (FIR form [6] or IIR form [7]) can all be modeled with bandpass filters [22]. This article chooses the strategy of the rotating frame sliding window filter (SWF), which is a kind of digital IIR filter. Its structure is depicted in Fig. 7. The dynamic response of the SWFs is defined as $U(s)$, and the dynamic of the kth harmonic's detection is defined as $D_k(s)$.

Apparently, $U(s)$ can be modeled as a transfer function in (4). Parameter T_1 is the time width of sliding window, which is set as the period of ac voltage in this article. According to

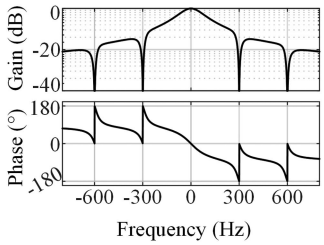

Fig. 8. Low-pass notch filter $F_{\rm dc}(s)$ of the APF's DVC controller.

the relationship between models under rotating frame and static frame [28], [29], [30], s in $U(s)$ is substituted with $(s-{\rm j}k\omega_1)$ to derive the model of $D_k(s)$. So HCD is modeled as (5)

$$U(s)=\frac{1-e^{-T_1 s}}{T_1 s} \tag{4}$$

$$\frac{i_{\rm ref}(s)}{i_{\rm L}(s)}=D(s)=\sum_k D_k(s)=\sum_k \frac{1-e^{-T_1(s-{\rm j}k\omega_1)}}{s-{\rm j}k\omega_1}. \tag{5}$$

In APF's control system, dc-voltage $v_{\rm dc}$ is an inner state. $v_{\rm dc}$ provides interacting paths for $v_{\rm g}$ and $i_{\rm L}$ to affect $i_{\rm c}$. These interacting paths depend on the harmonic steady state of the APF and introduce complicated frequency coupling effect [35], so they are difficult to describe precisely. However, this article finds out that the dc-associated interacting paths are ignorable compared with other paths [$G_{\rm i}(s)D(s)$ and $Y(s)$ in (2)] because of the APF's large dc-side capacitor.

The dc-voltage-related interacting paths can be described by (2), (6), and (7). Equation (6) explains the small-signal linearization result of the APF, where $C_{\rm apf}$ denotes the dc-side capacitor of APF. $V_{\rm dc}$, $V_{\rm g1}$, and I_{ck} are steady-state values of dc voltage, ac-bus voltage $v_{\rm g}$, and the kth harmonic in the APF's output current $i_{\rm c}$. $v_{\rm g}$ and harmonics in $i_{\rm c}$ are ac states, so $V_{\rm g1}$ and I_{ck} are complex values whose phases are based on $v_{\rm g}$. In (7), $H_{\rm dvc}(s)$ is the dc voltage controller, including a PI controller and a $6k$th (k=1,2,...) harmonic notch filter $F_{\rm dc}(s)$. $F_{\rm dc}(s)$ aims to prevent the steady-state $6\,k$th harmonic fluctuation in $v_{\rm dc}$ (which is inevitable because APF absorbs harmonic reactive power) from affecting $i_{\rm ref}$ and reducing precision of harmonic suppression. Bode plot of $F_{\rm dc}(s)$ is given in Fig. 8.

$$\begin{aligned} C_{\rm apf}v_{\rm dc}\frac{{\rm d}v_{\rm dc}}{{\rm d}t}&=-\frac{3}{2}\left(v_{{\rm g}\alpha}i_{{\rm c}\alpha}+v_{{\rm g}\beta}i_{{\rm c}\beta}\right)\xrightarrow{\text{Small-signal Linearization}}\\ C_{\rm apf}V_{\rm dc}\frac{{\rm d}\hat{v}_{\rm dc}}{{\rm d}t}&=-\frac{3}{4}\left(V_{\rm g1}e^{-{\rm j}\omega_1 t}\hat{i}_{\rm c}+V_{\rm g1}e^{{\rm j}\omega_1 t}\hat{i}_{\rm c}^{*}\right)\\ &\quad-\frac{3}{4}\left(\sum_k I_{ck}e^{{\rm j}k\omega_1 t}\hat{v}_{\rm g}^{*}+\sum_k I_{ck}^{*}e^{-{\rm j}k\omega_1 t}\hat{v}_{\rm g}\right) \end{aligned} \tag{6}$$

$$\hat{i}_{\rm ref}(s)=H_{\rm dvc}(s-{\rm j}\omega_1)L\{e^{{\rm j}\omega_1 t}\hat{v}_{\rm dc}\}$$

$$\text{where: } H_{\rm dvc}(s)=\left(K_{\rm dcp}+\frac{K_{\rm dci}}{s}\right)F_{\rm dc}(s). \tag{7}$$

DC-voltage-related paths are compared with other paths around the 5th harmonic ($5\omega_1$) here. If dc-voltage-related paths

TABLE I
MAJOR PARAMETERS OF THE APF TO EXPLAIN THE WEAK INFLUENCE OF DVC ON THE HARMONIC DYNAMIC

$L_{\rm f}(\mu{\rm H})$	400	$C_{\rm apf}({\rm mF})$	1.0
$K_{{\rm r},-5}$	1000	$K_{\rm p}$	4.0
$K_{\rm dcp}$	0.7	$K_{\rm dci}$	1.6
$V_{\rm g}$(V,rms value)	400	$V_{\rm dc}$(V)	800

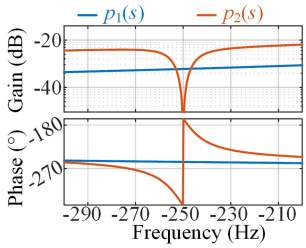

Fig. 9. Bode plots of $p_1(s)$ and $p_2(s)$.

are ignorable around $5\omega_1$, they will be absolutely ignorable around higher harmonics because of their low-pass characteristic. Based on the harmonic linearization [24], it is easy to derive $\hat{i}_{\rm c}(s)/\hat{v}_{\rm g}(s)$ and $\hat{i}_{\rm c}(s)/\hat{i}_{\rm L}(s)$ around $5\omega_1$, as shown in (8). $M_1=V_{\rm g1}/(0.5V_{\rm dc})$ is the steady state of APF's modulation wave, as defined in (2)

$$\begin{aligned} &\frac{\hat{i}_{\rm c}(s)}{\hat{v}_{\rm g}(s)}=\frac{Y(s)(1+(p_1(s))}{1+p_2(s)},\frac{\hat{i}_{\rm c}(s)}{\hat{i}_{\rm L}(s)}=\frac{D(s)G_{\rm i}(s)}{1+p_2(s)}\\ &p_1(s)=\frac{3I_{-11}^{*}\left[M_1+2H_{\rm dvc}(s-{\rm j}\omega_1)H_{\rm i}(s)\right]e^{-T_{\rm d}s}}{4V_{\rm dc}C_{\rm apf}(s-{\rm j}\omega_1)}\\ &p_2(s)=\frac{3\left[M_1^2Y(s)e^{-T_{\rm d}s}+2M_1H_{\rm dvc}(s-{\rm j}\omega_1)G_{\rm i}(s)\right]}{8C_{\rm apf}(s-{\rm j}\omega_1)}. \end{aligned} \tag{8}$$

In (8), $p_1(s)$ and $p_2(s)$ reflect dc-voltage-related paths. If $|p_1(s)|$ and $|p_2(s)|$ are both much smaller than 1.0, these paths can be ignored. From (8), the smaller $C_{\rm apf}$ or higher I_{-11} is, the larger $|p_1(s)|$ and $|p_2(s)|$ are. For a 30 kVA APF that suppresses $(6k\pm1)$th harmonics, the smallest value of $C_{\rm apf}$ is given with other key parameters in Table I. Under these parameters, when the APF outputs 5th harmonic current in full rated power, the 6th harmonic fluctuation of $v_{\rm dc}$ gets to 80 Vpp, which is one-tenth of $V_{\rm dc}$.

To make $|p_1(s)|$ as large as possible to show that it is ignorable, the APF is assumed to output -11th harmonic current with full rated power ($|I_{{\rm c},-11}^{*}|=58$ A). Under this condition, bode plots of $p_1(s)$ and $p_2(s)$ are given in Fig. 9. Apparently, $|p_1(s)|$ and $|p_2(s)|$ are both much lower than 0 dB, so dc voltage related paths in the APF control system are ignorable compared with other major interacting paths.

In conclusion, the small-signal model of APF can be simplified into (9) in harmonic stability assessment. $G_{\rm i}(s)$, $D(s)$ and $Y(s)$ are given in (2), (3), and (5). As a result, APF can be considered a 2-in-1-out linear-time-invariant (LTI) system

$$\hat{i}_{\rm c}(s)=G_{\rm i}(s)D(s)\hat{i}_{\rm L}(s)-Y(s)\hat{v}_{\rm g}(s). \tag{9}$$

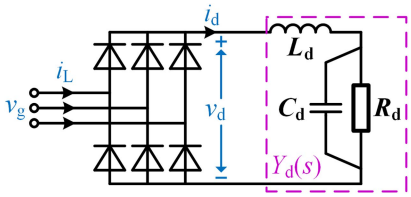

Fig. 10. Topology of the diode rectifier.

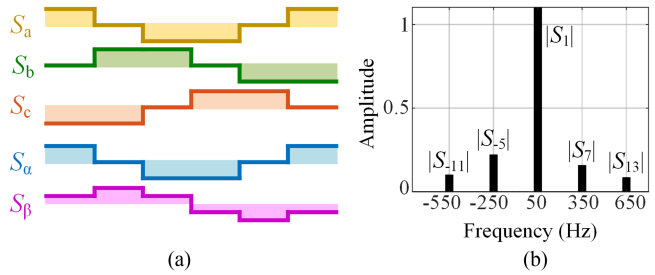

Fig. 11. Waveforms and spectrum of the switching functions.

B. Modeling of the Nonlinear Load

A 6-pulse diode rectifier is chosen as the nonlinear load in this article. The topology is given in Fig. 10. Two internal states, dc-side current i_d and voltage v_d, are defined. $Y_d(s)$ denotes dc-side admittance, whose unit pulse response is $y_d(t)$.

Relationships among v_g, i_L, v_d, and i_d can be described by (10). Switching functions S_a, S_b, S_c are defined in (11)

$$\begin{cases} \hat{v}_d(t) = S_a(t)v_a(t) + S_b(t)v_b(t) + S_c(t)v_c(t) \\ [i_a(t)\ i_b(t)\ i_c(t)] = [S_a(t)\ S_b(t)\ S_c(t)]\, i_d(t) \\ i_d(t) = y_d(t) * v_d(t) \end{cases} \tag{10}$$

$$S_x = \begin{cases} 1, & \text{upper diode on} \\ -1, & \text{bottom diode on} \\ 0, & \text{both diode off.} \end{cases} \tag{11}$$

Under the condition of current-continues mode and ignoring commutating-delay angle (CDA), S_a, S_b, S_c can be considered periodical square-wave signals independent of current. As a result, the rectifier is nearly a linear-time-periodically variant (LTP) system [33]. This article is aimed at stability assessment of the APF system, so small-signal dynamic characteristic (small-signal admittance from ac-bus voltage v_g to the rectifier's input current i_L) is mainly cared about.

The model of the 6-pulse rectifier should be transformed to the same form (complex form [32]) as the model of APF, where the variables' real part denotes the α-axis component and the imaginary part denotes the β-axis component. Equation (10) is transformed into $\alpha\beta$ frame in (12). Then the $\alpha\beta$ form model is further transformed into complex form in (13). The sign "*" in this article means convolution

$$\begin{cases} \hat{v}_d = 1.5(S_\alpha \hat{v}_\alpha + S_\beta \hat{v}_\beta) \\ (\hat{i}_{L\alpha}, \hat{i}_{L\beta})^T = \hat{i}_d (S_\alpha, S_\beta)^T \end{cases}, \quad \hat{i}_d(s) = Y_d(s)\hat{v}_d(s) \tag{12}$$

$$\hat{i}_L = \frac{3}{4} S_{\alpha\beta}(t) \left[y_d(t) * (S_{\alpha\beta}(t)\hat{v}_g^* + S_{\alpha\beta}^*(t)\hat{v}_g) \right]. \tag{13}$$

To explain the harmonic information of $S_{\alpha\beta}$, waveforms of the switching signals are given in Fig. 11(a). Based on the waveforms, it is easy to do the Fourier integration [as shown in (14)] to obtain the analytical spectrum of $S_{\alpha\beta}$ as shown in (15). The footnote k denotes the kth harmonic. Based on (15), $|S_k|$ is given in Fig. 11(b)

$$S_k = \frac{1}{T_1} \int_0^{T_1} (S_\alpha(t) + \mathrm{j} S_\beta(t))\, e^{-\mathrm{j}k\omega_1 t} \mathrm{d}t \tag{14}$$

$$S_k = \frac{(-1)^k - 1}{\sqrt{3}\pi k} \left(e^{-\mathrm{j}\frac{\pi}{3}(k+2)} + e^{-\mathrm{j}\frac{\pi}{3}(2k+1)} - 1 \right). \tag{15}$$

$|S_1|$ is much larger than $|S_k|$ $(k \neq 1)$. According to the harmonic linearization theory [24], the most significant component in the modulation signals of a LTP system mainly determines the dynamic characteristic. So for simplicity, $|S_k|$ $(k \neq 1)$ are ignored in this article, which means $S_{\alpha\beta}(t)$ is considered approximately $S_1 e^{\mathrm{j}\omega_1 t}$. Then, based on (15), (13) can be further simplified as follows:

$$\hat{i}_L = \frac{9}{\pi^2} \left(y_d(t) e^{\mathrm{j}\omega_1 t} \right) * \left(e^{\mathrm{j}2\omega_1 t} \hat{v}_g^* + \hat{v}_g \right). \tag{16}$$

A fundamental frequency modulation factor $e^{\mathrm{j}2\omega_1 t}$ appears in the model (16), which is similar to the model of VSCs in [30]. The modulation factor $e^{\mathrm{j}2\omega_1 t}$ is caused by the asymmetry of the model on *d*- and *q*- axes. For a 6-pulse rectifier, the asymmetry reflects the coupling between the *d*/*q* axis voltage/current and v_{dc}. The result of $e^{\mathrm{j}2\omega_1 t}$ is a frequency coupling effect between positive and negative sequence signals. For example, if a voltage perturbation $\hat{v}_{gp}$ (the frequency is ω_p) exists in v_g, the response signal of i_L will contain frequency components of $\hat{i}_{Lp}$ (ω_p) and $\hat{i}_{Ln}$ $(2\omega_1 - \omega_p)$. To describe the frequency coupling with LTI expressions, v_g and i_L are decomposed into positive and negative sequence components, as shown in (17). By substituting (17) into (16), modulation factor $e^{\mathrm{j}2\omega_1 t}$ is eliminated, as shown in (18). Then an 2-in-2-out LTI input admittance matrix is obtained as (19), which is convenient for stability assessment

$$\hat{i}_L = \hat{i}_{Lp} + e^{\mathrm{j}2\omega_1 t} \hat{i}_{Ln}^*, \quad \hat{v}_g = \hat{v}_{gp} + e^{\mathrm{j}2\omega_1 t} \hat{v}_{gn}^* \tag{17}$$

$$\begin{cases} \hat{i}_{Lp} = \frac{9}{\pi^2} \left(y_d(t) e^{\mathrm{j}\omega_1 t} \right) * (\hat{v}_{gn} + \hat{v}_{gp}) \\ \hat{i}_{Ln} = \frac{9}{\pi^2} \left(y_d(t) e^{\mathrm{j}\omega_1 t} \right) * (\hat{v}_{gn} + \hat{v}_{gp}) \end{cases} \tag{18}$$

$$\begin{bmatrix} \hat{i}_{Lp}(s) \\ \hat{i}_{Ln}(s) \end{bmatrix} = \frac{9}{\pi^2} Y_d(s - \mathrm{j}\omega_1) \begin{bmatrix} 1 & 1 \\ 1 & 1 \end{bmatrix} \begin{bmatrix} \hat{v}_{gp}(s) \\ \hat{v}_{gn}(s) \end{bmatrix}. \tag{19}$$

Two more points should be stressed. First, ignorance of diodes' commutation delay angle (CDA) does not degrade the precision of the model, because CDA has little influence on S_1 and does not increase harmonic components of $S_{\alpha\beta}(t)$. An example of CDA $= 20°$ is given here to show CDA's impact on $|S_k|$. $S_{a/b/c}(t)$ differentiates into the current switching function $S_{ia/b/c}(t)$ [to replace $S_{a/b/c}(t)$ in the second equation of (10)] and voltage switching function $S_{ua/b/c}(t)$ [to replace $S_{a/b/c}(t)$ in the first equation of (10)] [26], [27], as shown in Fig. 12(a). Spectrums of $S_a(t)$, $S_{ia}(t)$, and $S_{ua}(t)$ are shown in Fig. 12(b). So the influence of CDA is not apparent.

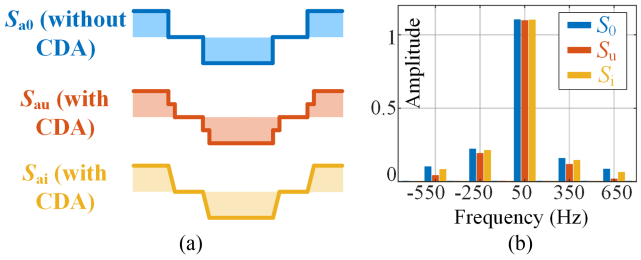

Fig. 12. Waveforms and spectrums of the switching functions with/without commutation delay angle.

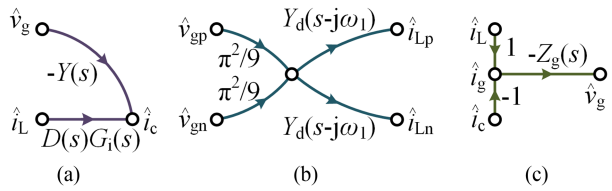

Fig. 13. Small-signal models of each part in the APF system in signal-flow diagrams.

Second, modeling approach of this article can also be applied to other semicontrolled or noncontrolled nonlinear loads, by modifying switching functions accordingly. For example, the difference between thyristor and diode rectifier is the firing angle. So, a model of a thyristor rectifier is obtained by replacing $S_{\alpha\beta}(t)$ with $S_{\alpha\beta}(t) * \delta(t - \alpha/\omega_1)$ in (13). $\delta(t)$ denotes the unity-pulse signal and α denotes the firing angle.

IV. Stability Analyzing of the APF System

A. Model Combination of the APF, Nonlinear Load and Grid Impedance

In this section, the models derived in Section III are utilized to assess the stability of the APF system shown in Fig. 1. Dynamic interaction within the APF system is described by the combination of the models.

For clarity, signal flow diagrams of the models are listed in Fig. 13. i_c and i_g are decomposed into positive and negative sequence components just like v_g and i_L in the model of 6-pulse rectifier (17). Then the models are connected together, as shown in Fig. 14.

Positive and negative loops are conjugate symmetric about $j\omega_1$. In the APF system, 6-pulse rectifier is the junction that relates positive and negative sequence loop gain together. Correspondingly, the system characteristic polynomial is the sum of positive, negative loop gain ($T_p(s)$, $T_p^*(s^* + j2\omega_1)$), and 1, as shown in the following:

$$\Delta(s) = 1 + \underbrace{T_p(s) + T_p^*(s^* + j2\omega_1)}_{T(s)}$$

$$\text{where: } T_p(s) = \frac{9}{\pi^2} Y_d(s - j\omega_1) \frac{Z_g(s)\left[1 - D(s)G_i(s)\right]}{1 + Z_g(s)Y(s)}. \tag{20}$$

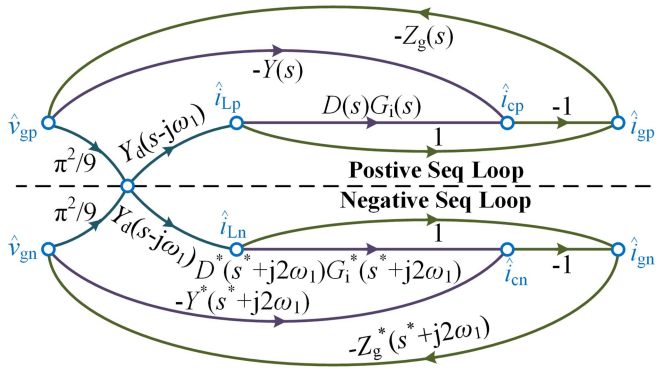

Fig. 14. Combination of each part's small-signal models in a signal-flow diagram.

TABLE II
Parameters of the APF System for Stability Analyzing

$L(\mu H)$	800	$C(\mu F)$	150	$R(\Omega)$	0.9
$L_d(\mu H)$	1200	$C_d(\mu F)$	100	$R_d(\Omega)$	20
$L_f(\mu H)$	400	K_p	3.8	K_r	1000

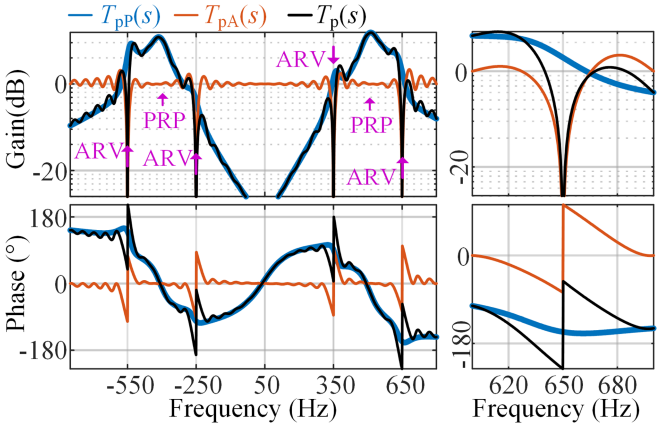

Fig. 15. Bode plots of $T_{pP}(s)$, $T_{pA}(s)$, and $T_p(s)$.

According to the Nyquist criterion [34], if $\angle T(s)$ crosses $\pm 180°$ at ω_c where $|T(s)| > 1$, characteristic equation $\Delta(s) = 0$ will have a right-half-plane root, which means the APF system will have an unstable dynamic mode around $j\omega_c$. So this article utilizes $T(s)$ to assess stability.

Sequence loop gain $T_p(s)$ can be decomposed into two factors, the active factor $T_{pA}(s)$ and the passive factor $T_{pP}(s)$, as shown in (21). $T_{pP}(s)$ reflects the dynamic of passive components in the APF system. Whereas $T_{pA}(s)$ describes the dynamic of APF's harmonic detection and closed-loop current control

$$T_{pP}(s) = \frac{9}{\pi^2} \frac{Z_g(s)Y_d(s - j\omega_1)}{1 + Z_g(s)Y(s)}, \quad T_{pA}(s) = 1 - D(s)G_i(s). \tag{21}$$

A case study is given to reveal how the interaction influences stability. Major parameters are listed in Table II. Bode plots of $T_{pP}(s)$, $T_{pA}(s)$, and $T_p(s)$ are given in Fig. 15.

$T_{pP}(s)$ has two passive resonance peaks (PRP) at the resonance frequency of $\pi^2/9 * Y_d(s - j\omega_1)Z_g(s)$. $T_{pA}(s)$ has active

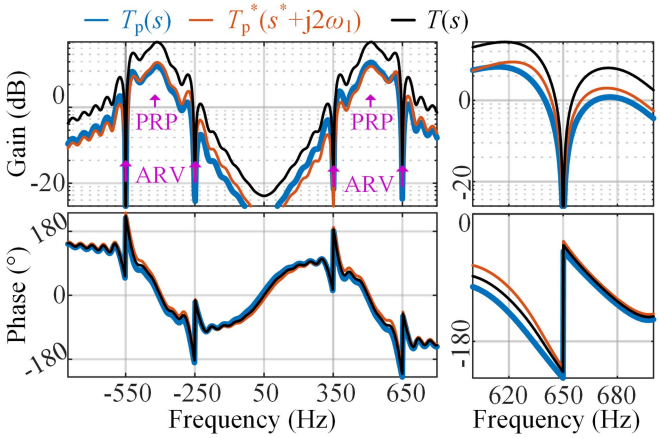

Fig. 16. Bode plots of $T(s)$, $T_{\rm p}(s)$, and $T_{\rm p}^*(s^*+{\rm j}2\omega_1)$ in symmetric condition.

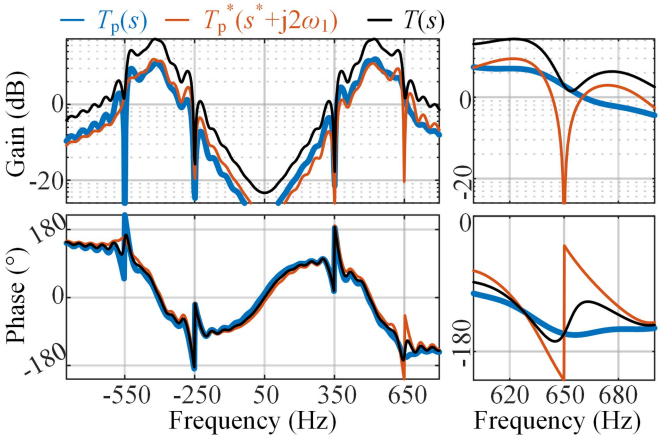

Fig. 18. Bode plots of $T(s)$, $T_{\rm p}(s)$ and $T_{\rm p}^*(s^*+{\rm j}2\omega_1)$ when 13th harmonic suppression is canceled.

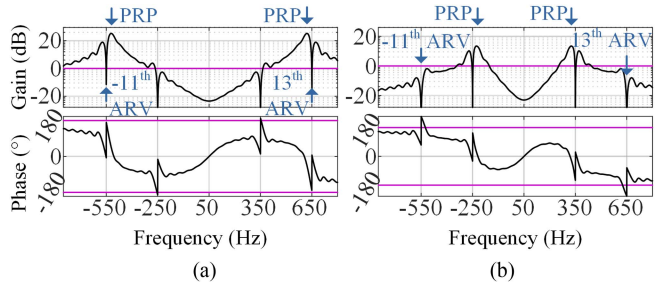

Fig. 17. Bode plots of $D(s)$, $G_{\rm i}(s)$, and $D(s)G_{\rm i}(s)$.

resonance valleys (ARV) at suppressed harmonics. $\angle T_{\rm pP}(s)$ gets close to $\pm 180^\circ$ quickly as frequency increases around PRPs, and $|T_{\rm pP}(s)|$ bumps there. Meanwhile, $\angle T_{\rm pA}(s)$ falls and rises rapidly around ARVs.

When a PRP gets close to an ARV, phase shifting of ARV and gain bump, phase deviation of PRP are added together, which is easy to make $\angle T_{\rm p}(s)$ cross $\pm 180^\circ$. As shown in Fig. 15, $\angle T_{\rm p}(s)$ crosses $\pm 180^\circ$ around $-11\omega_1$ and $13\omega_1$, and the phase crossing point is located where $|T_{\rm p}(s)| > 1$.

The whole loop gain $T(s)$ is the sum of $T_{\rm p}(s)$ and $T_{\rm p}^*(s^* + {\rm j}2\omega_1)$. Their bode plots are given in Fig. 16. So $\angle T(s)$ crosses $\pm 180^\circ$ where $|T(s)| > 1$. As a result, the APF system is unstable and has -11th/13th harmonic oscillation, just like the example in Fig. 4.

If the passive resonance peaks move to higher or lower frequencies, the APF system may get stable, as shown in Fig. 17. When PRPs move to a higher frequency, $\angle T(s)$ moves away from $\pm 180^\circ$, which results in phase margin. When PRPs move to a lower frequency, $|T(s)|$ gets lower, which results in gain margin.

In conclusion, "PRPs getting close to ARVs" activates the propensity of the APF system's harmonic oscillation.

Some questions still need investigation. First, the difference of $T_{\rm p}(s)$ and $T(s)$ is not considered, which reflects exactly the frequency coupling effect introduced by the nonlinear load. Second, how the CIC parameters influence $T_{\rm pA}(s)$ and $Y(s)$ is unknown. The following two subsections discuss the two questions.

B. Influence of Nonlinear Load's Frequency Coupling Effect

If frequency coupling was ignored, the characteristic polynomial $\Delta(s)$ would be $1 + 2T_{\rm p}(s)$ rather than that in (20). As shown in Fig. 16, $T_{\rm p}(s)$ is similar to $T_{\rm p}^*(s^* + {\rm j}2\omega_1)$, so ignoring frequency coupling may not result in apparent imprecision in this situation.

The similarity of $T_{\rm p}(s)$ and $T_{\rm p}^*(s^* + {\rm j}2\omega_1)$ is because of the symmetry of harmonic suppression. If 13th harmonic suppression is canceled but -11th harmonic suppression is remained, $T_{\rm p}(s)$ and $T_{\rm p}^*(s^* + {\rm j}2\omega_1)$ will be apparently different from each other around $-11\omega_1$ and $13\omega_1$, as shown in Fig. 18.

$T_{\rm p}(s)$ gets smooth around $13\omega_1$ and does not cross -180°, but is sharp around $-11\omega_1$ and crosses 180°. Inversely, $T_{\rm p}^*(s^* + {\rm j}2\omega_1)$ is smooth around $-11\omega_1$ but sharp around $13\omega_1$. If frequency coupling was ignored, so only $T_{\rm p}(s)$ was used to assess the stability, the APF system would be believed to have unstable dynamic mode around $-{\rm j}11\omega_1$. However, according to $T(s)$ in Fig. 18, the APF system is stable in fact.

The reason for being stable is that the damping effect ($T_{\rm p}(s)$ getting smooth around $13\omega_1$) is brought to the -11th harmonic through the frequency coupling. This example indicates that frequency coupling is necessary to consider for stability assessment. Otherwise, one may obtain imprecise conclusions.

$T(s)$ is symmetric, which means $T(s) = T^*(s^* + {\rm j}2\omega_1)$. Therefore, if the APF system has an unstable mode around $k\omega_1$, it must have another unstable mode around $(2-k)\omega_1$. So kth and $(2-k)$th harmonics share their resonance characteristic in the APF system.

C. Influences of Current Inner-Loop Controller

CIC controller $H_{\rm i}(s)$ influences the dynamic interaction of the APF system in two aspects. First, $H_{\rm i}(s)$ affects the active loop-gain factor $T_{\rm pA}(s)$ through the current dynamic response

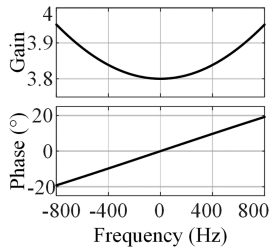

Fig. 19. Bode plots of $L_{\rm f}s + K_{\rm p}e^{-T_{\rm d}s}$.

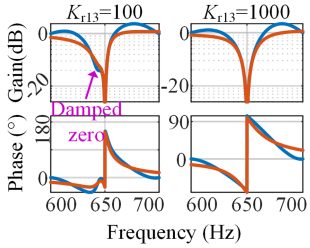

Fig. 20. Comparison of $T_{\rm pA}(s)$ and $T_{\rm pASim}(s)$.

$G_{\rm i}(s)$. Second, $H_{\rm i}(s)$ influences passive loop-gain factor $T_{\rm pP}(s)$ through APF input admittance $Y(s)$.

As shown in (3), CIC includes a proportional controller $K_{\rm p}$ and resonance controllers $R_k(s)$. $R_k(s)$ aims to eliminate steady-state harmonic components in current error $(i_{\rm ref} - i_{\rm c})$. $\varphi_{{\rm r}k}$ is set to cancel out digital control delay and $K_{{\rm r}k}$ determines the bandwidth of the kth harmonic control.

According to Section IV-A, the kth harmonic stability is reflected by $T(s)$ around $k\omega_1$. Meanwhile, around $k\omega_1$, $|R_i(s)|$ and $|D_i(s)|$ $(i \neq k)$ are so small that they can be ignored. Therefore, the approximation in (22) is reasonable to simplify the stability assessment

$$H_{\rm i}(s) \approx K_{\rm p} + R_k(s), \quad D(s) \approx D_k(s) = \frac{1 - e^{-T_1(s-{\rm j}k\omega_1)}}{T_1(s-{\rm j}k\omega_1)}. \tag{22}$$

The complex exponential function in $D_k(s)$ is not convenient for analysis. So it is approximated to a rational function around $k\omega_1$, as shown in (23). Then the active factor $T_{\rm pA}(s)$ can be approximated to $T_{\rm pASim}(s)$ around $k\omega_1$, as shown in (24). Zeros and poles of (24) are given in (25)

$$e^{-T_1(s-{\rm j}k\omega_1)} = \frac{e^{-0.5T_1(s-{\rm j}k\omega_1)}}{e^{0.5T_1(s-{\rm j}k\omega_1)}} \approx \frac{1 - 0.5(T_1 s - {\rm j}2k\pi)}{1 + 0.5(T_1 s - {\rm j}2k\pi)}$$

$$\Rightarrow 1 - e^{-T_1(s-{\rm j}k\omega_1)} \approx \frac{2(s-{\rm j}k\omega_1)}{\omega_1/\pi + (s-{\rm j}k\omega_1)} \tag{23}$$

$$T_{\rm pA}(s) \overset{s\approx {\rm j}k\omega_1}{\approx} T_{\rm pASim}(s) = \left(1 + \frac{\omega_1 L_{\rm f}}{\pi K_{\rm p} e^{{\rm j}\varphi(s)}}\right) \frac{s-z_1}{s-p_1}\frac{s-z_2}{s-p_2} \tag{24}$$

$$z_1 = \frac{{\rm j}k\omega_1 - K_{{\rm r}k}/(K_{\rm p}e^{{\rm j}\varphi(s)})}{1 + \omega_1 L_{\rm f}/(\pi K_{\rm p} e^{{\rm j}\varphi(s)})}, \quad z_2 = {\rm j}k\omega_1$$

$$p_1 = {\rm j}k\omega_1 - \frac{K_{{\rm r}k}}{K_{\rm p}e^{{\rm j}\varphi(s)}}, \quad p_2 = {\rm j}k\omega_1 - \frac{\omega_1}{\pi}. \tag{25}$$

The factor $(L_{\rm f}s + K_{\rm p}e^{-T_{\rm d}s})$ is approximated to $K_{\rm p}e^{{\rm j}\varphi(s)}$, where $\varphi(s)$ is a small phase deviation. Bode plot of $(L_{\rm f}s + K_{\rm p}e^{-T_{\rm d}s})$ is given in Fig. 19 to show this approximation is reasonable. $T_{\rm pA}(s)$ and $T_{\rm pASim}(s)$ are compared in Fig. 20. So the approximation is precise enough for stability assessment.

According to (25), when $K_{{\rm r}k}$ is large, p_1 and z_1 are on the left half plane and far from the imaginary axis. So $T_{\rm pA}(s)$ mainly depends on p_2 and z_2. But when $K_{{\rm r}k}$ decreases to a small value that is compatible with $K_{\rm p}k\omega_1$, p_1 and z_1 will move to the right.

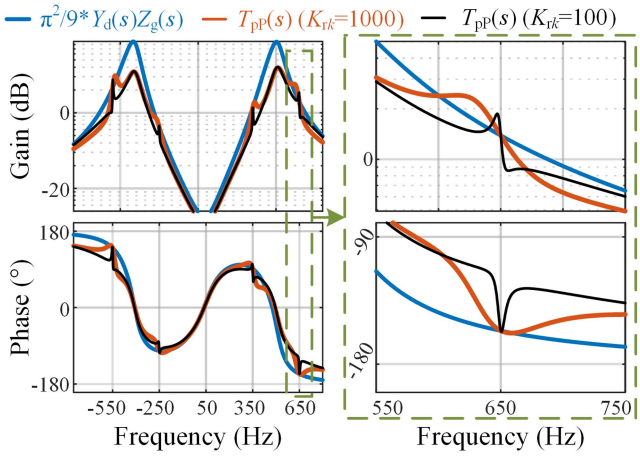

Fig. 21. Comparison of $T_{\rm pP}(s)$ and $\frac{\pi^2}{9}Z_{\rm g}(s)Y_{\rm d}(s-{\rm j}\omega_1)$.

p_1 gets close to z_2 to cause quasi pole-zero cancellation that makes the kth ARV narrower. Meanwhile, the LHP damped zero z_1 provides phase leading for $T_{\rm pA}(s)$, as shown in Fig. 20. So reducing $K_{{\rm r}k}$ introduces phase leading that is good for the kth harmonic stability.

With the approximation in (22), $Y(s)$ is simplified to (26) around $k\omega_1$. Away from $k\omega_1$, $Y(s)$ is almost resistive, so it can operate as an active damper if $K_{{\rm r}k}$ is set small enough. As shown in Fig. 21, compared with $\pi^2/9 * Z_{\rm g}(s)Y_{\rm d}(s-{\rm j}\omega_1)$, $T_{\rm pP}(s)$ is further away from $\pm 180°$ because of the damping effect of $Y(s)$. And the smaller $K_{{\rm r}k}$ is, the stronger the damping effect is

$$Y(s) = -\frac{1}{L_{\rm f}s + K_{\rm p}e^{-T_{\rm d}s} + \frac{K_{{\rm r}k}e^{{\rm j}\varphi_{{\rm r}k}}}{s-{\rm j}k\omega_1}e^{-T_{\rm d}s}}. \tag{26}$$

So reducing $K_{{\rm r}k}$ benefits the kth harmonic stability according to its impacts on $T_{\rm pP}(s)$ and $T_{\rm pA}(s)$. However, negative sequence loop gain $T_{\rm p}^*(s^* + {\rm j}2\omega_1)$ also influences the stability. As shown in Fig. 22(a), the APF system is still unstable when only $K_{\rm r13}$ is reduced.

So for effective improvement if the stability of the kth harmonic, both $K_{{\rm r}k}$ and $K_{{\rm r},2-k}$ should be reduced to a small value. Fig. 22(b) indicates that the APF system is stabilized by reducing $K_{{\rm r},-11}$ and $K_{\rm r13}$ together.

Although reducing $K_{{\rm r}k}$ benefits the stability, it may also lead to unacceptable dynamic performance degradation. So $K_{{\rm r}k}$ is seldom set to a low value.

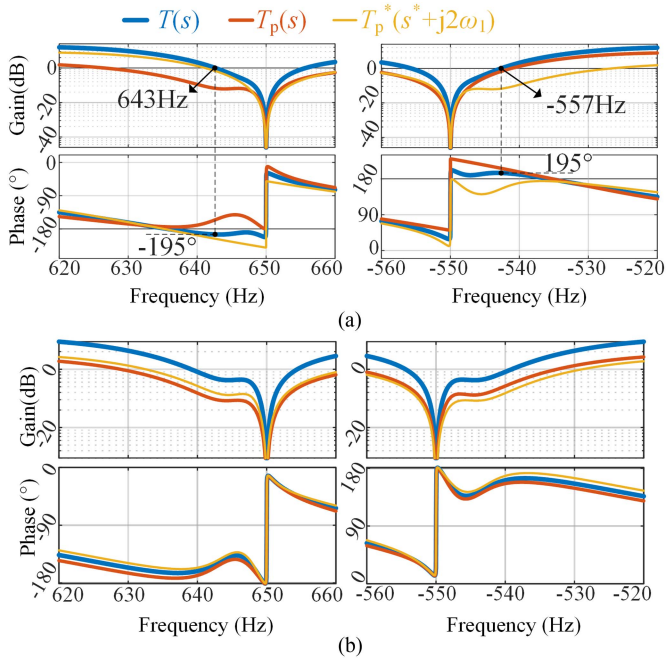

Fig. 22. Bode plots of $T(s)$, $T_{\mathrm{p}}(s)$, and $T_{\mathrm{p}}^{*}(s^{*}+\mathrm{j}2\omega_1)$ when reducing $K_{\mathrm{r}13}$ or $K_{\mathrm{r},-11}$. (a) Reduce $K_{\mathrm{r}13}$ only. (b) Reduce $K_{\mathrm{r}13}$ and $K_{\mathrm{r},-11}$.

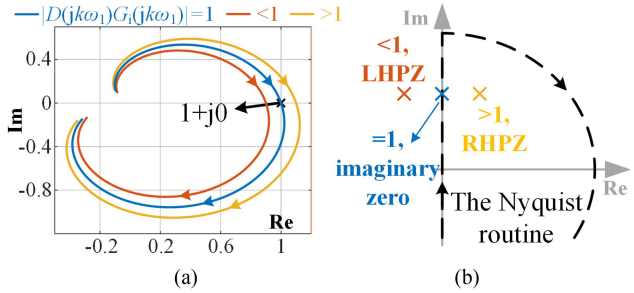

Fig. 23. Nyquist plot of $D(s)G_{\mathrm{i}}(s)$ and open-loop zeros' locations of the active part when $|D(\mathrm{j}k\omega_1)G_{\mathrm{i}}(\mathrm{j}k\omega_1)|$ varies. (a) Nyquist plot of different $D(s)G_{\mathrm{i}}(s)$ around $k\omega_1$. (b) Positions of the Nyquist routine and major zeros.

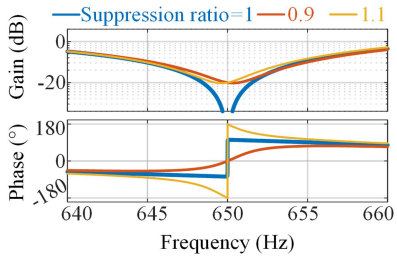

Fig. 24. Bode plots of $T_{\mathrm{pA}}(s)$ when $|D(\mathrm{j}k\omega_1)G_{\mathrm{i}}(\mathrm{j}k\omega_1)|$ varies.

V. Reassessment of APF's Stabilizing Methods

According to Section IV-A, grid-side impedance $Z_{\mathrm{g}}(s)$ and load admittance $Y_{\mathrm{d}}(s)$ determine harmonic resonance stability. Unfortunately, $Z_{\mathrm{g}}(s)$ and $Y_{\mathrm{d}}(s)$ are usually unknown and varying, so harmonic oscillation is challenging to avoid in the APF designing stage and stabilizing methods are in need for APF systems. Widely used stabilizing methods are harmonic suppressing ratio reduction (SSR) [21], [22] and harmonic virtual admittance (HVA) [20]. However, the frequency coupling effect introduced by the nonlinear load is seldom considered when designing the above two methods. The ignorance of frequency coupling may lead to ineffective or over-damped (low suppression precision or dynamic) harmonic stabilization. So in this section, SSR and HVA are reassessed, considering the frequency coupling effect, to provide a theoretical guidance for choosing and parameter designing of them.

A. Suppression Ratio Reducing (SRR)

Suppressing ratio $K_{\mathrm{SR}k}$ is the ratio of kth harmonic component within i_{ref} to load current i_{L}, which is a configurable control parameter. $K_{\mathrm{SR}k}$ is modeled as a proportional gain in cascade with HCD, often set to 1.0 for precise harmonic suppression. $K_{\mathrm{SR}k}$ only influences $T_{\mathrm{pA}}(s)$ in the model, as shown in the following:

$$T_{\mathrm{pA}}(s)=1-\sum_{k}K_{\mathrm{SR}k}D_k(s)G_{\mathrm{i}}(s). \tag{27}$$

$T_{\mathrm{pA}}(s)$ has a series of zeros around $\mathrm{j}k\omega_1$ on the complex plane, coinciding with ARVs. As shown in Fig. 23, when $K_{\mathrm{SR}k}=1$, Nyquist curve of $T_{\mathrm{pA}}(s)$ crosses 1+j0, so, the corresponding zero is on the imaginary axis according to the mapping principle, making $|T_{\mathrm{pA}}(\mathrm{j}k\omega_1)|=0$. The zero reflects the parallel resonance mentioned in Section II. The corresponding bode plot of $T_{\mathrm{pA}}(s)$ is shown in Fig. 24.

If $K_{\mathrm{SR}k}>1$ (harmonic over suppression), the Nyquist curve will expand and encircle the origin, as shown in Fig. 23(a). Then the zero will move inside the Nyquist routine and become a right-half plane (RHP) zero, introducing an antidamping effect to the aforementioned parallel resonance as shown in Fig. 24. The dramatic phase stepping at $k\omega_1$ makes $T_{\mathrm{p}}(s)$ easy to cross $\pm180°$. So $K_{\mathrm{SR}k}$ is seldom set larger than 1.0.

Oppositely, if $K_{\mathrm{SR}k}<1$, the Nyquist plot will shrink and not encircle the origin. The zero of $T_{\mathrm{pA}}(s)$ around $k\omega_1$ will move outside the Nyquist routine and become a left-half-plane (LHP) zero, which damps the parallel resonance and improves the stability margin, as shown in Fig. 24.

According to the frequency coupling, this article finds out that reducing $K_{\mathrm{SR}k}$ damps APF system around both $k\omega_1$ and $(2-k)\omega_1$. Bode plots of positive and negative sequence loop gain ($T_{\mathrm{p}}(s)$, $T_{\mathrm{p}}^{*}(s^{*}+\mathrm{j}2\omega_1)$) around $k\omega_1$ is given in Fig. 25. Reducing $K_{\mathrm{SR}k}$ to 0.4 dampens $T_{\mathrm{p}}(s)$ around $k\omega_1$, whereas $T_{\mathrm{p}}^{*}(s^{*}+\mathrm{j}2\omega_1)$ is not dampened. Dampened $|T_{\mathrm{p}}(s)|$ is much larger than undampened $|T_{\mathrm{p}}^{*}(s^{*}+\mathrm{j}2\omega_1)|$. As a result, dampened $|T_{\mathrm{p}}(s)|$ dominates the whole equivalent loop gain $T(s)$.

A frequency ω' is chosen, and $T_{\mathrm{p}}(\mathrm{j}\omega')$, $T_{\mathrm{p}}^{*}(-\mathrm{j}\omega'+\mathrm{j}2\omega_1)$ are depicted as vectors as shown in Fig. 26. After reducing $K_{\mathrm{SR}13}$, $\angle T_{\mathrm{p}}(\mathrm{j}\omega')$ is no longer lower than $-180°$ and $|T_{\mathrm{p}}(\mathrm{j}\omega')|$ is one time larger than $|T_{\mathrm{p}}^{*}(-\mathrm{j}\omega'+\mathrm{j}2\omega_1)|$. So $T(s)$ is attracted toward $|T_{\mathrm{p}}(\mathrm{j}\omega')|$ and gets a certain phase stable margin.

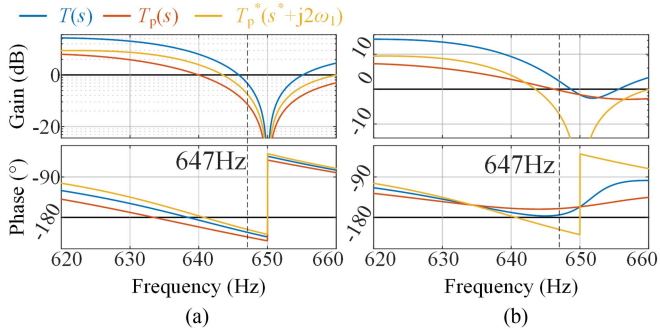

Fig. 25. Bode plots of $T_{\mathrm{p}}(s)$, $T_{\mathrm{p}}^{*}(s^{*}+\mathrm{j}2\omega_1)$ and $T(s)$ before and after reducing K_{SR13} from 1.0 to 0.4. (a) Before reducing. (b) After reducing.

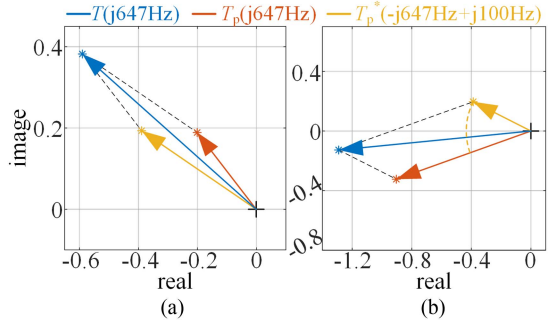

Fig. 26. Vector plots of $T_{\mathrm{p}}(\mathrm{j}647\,\mathrm{Hz})$, $T_{\mathrm{p}}(-\mathrm{j}647\mathrm{Hz}+\mathrm{j}100\,\mathrm{Hz})$ and $T(\mathrm{j}647\,\mathrm{Hz})$ before and after changing K_{SR13} from 1.0 to 0.4. (a) Before reducing. (b) After reducing.

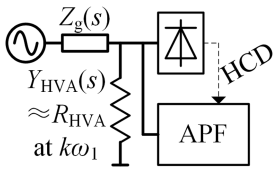

Fig. 27. Basic idea of HVA.

In conclusion, thanks to the frequency coupling effect caused by the nonlinear load, SRR can stabilize kth and $(2-k)$th harmonic oscillations simultaneously.

B. Harmonic Virtual Admittance (HVA) Control

Introducing resistive admittance R_{HVA} into the APF system can reduce the phase deviation of $\angle T_{\mathrm{pP}}(s)$ so benefits the stability, as shown in Fig. 27. But the real resistor causes unacceptable power loss, so R_{HVA} is usually realized by a virtual admittance control strategy within the APF control system, as shown in Fig. 28.

The transfer function of $A(s)$ is given in (28), and a different equation of $A_k(s)$ is given in (29) to show the digital realization of HVA. $A_k(s)$ is a bandpass filter tuned to be aligned with $k\omega_1$. So, the suppressed harmonics in v_{g} cause in-phase harmonics in

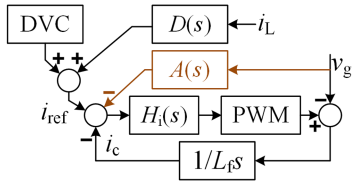

Fig. 28. Block diagram of HVA.

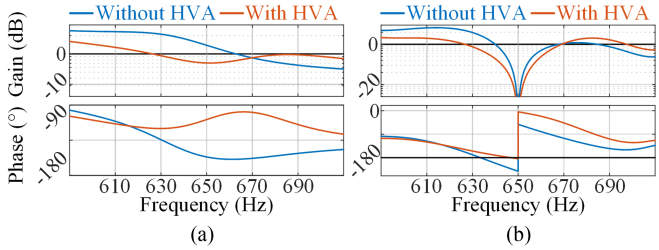

Fig. 29. Bode plots of $T_{\mathrm{pP}}(s)$ and $T_{\mathrm{p}}(s)$ with/without HVA control. (a) $T_{\mathrm{pP}}(s)$. (b) $T_{\mathrm{p}}(s)$.

i_{c}, which means resistive admittance of APF

$$A(s)=\sum_k A_k(s)=\sum_k \frac{K_{\mathrm{VA}k}\sigma_k}{s-\mathrm{j}k\omega_1+\sigma_k} \tag{28}$$

$$\begin{cases} y_\alpha[k]=A_{\mathrm{HVA}}y_\alpha[k-1]-B_{\mathrm{HVA}}y_\beta[k-1]+C_{\mathrm{HVA}}u_\alpha[k] \\ y_\beta[k]=B_{\mathrm{HVA}}y_\alpha[k-1]+A_{\mathrm{HVA}}y_\beta[k-1]+C_{\mathrm{HVA}}u_\beta[k] \end{cases}$$

$$A_{\mathrm{HVA}}=e^{-\sigma_k T_{\mathrm{s}}}\cos(k\omega_1 T_{\mathrm{s}}),\ B_{\mathrm{HVA}}=e^{-\sigma_k T_{\mathrm{s}}}\sin(k\omega_1 T_{\mathrm{s}}),$$

$$C_{\mathrm{HVA}}=K_{\mathrm{VA}k}\sigma_k T_{\mathrm{s}}. \tag{29}$$

With HVA applied, the admittance of APF is improved from $Y(s)$ to $Y_{\mathrm{Imp}}(s)$, as shown in (30). Within bandwidth of CIC (several kHz), $|H_{\mathrm{i}}(s)|$ is much larger than $|L_{\mathrm{f}}s|$, so the $Y_{\mathrm{HVA}}(s)$ and $Y_{\mathrm{Imp}}(s)$ are almost resistive around harmonics under suppression

$$\begin{aligned} Y_{\mathrm{Imp}}(s)&=Y(s)+Y_{\mathrm{HVA}}(s) \\ &=\frac{1}{L_{\mathrm{f}}s+H_{\mathrm{i}}(s)e^{-T_{\mathrm{d}}s}}+\frac{A(s)H_{\mathrm{i}}(s)e^{-T_{\mathrm{d}}s}}{L_{\mathrm{f}}s+H_{\mathrm{i}}(s)e^{-T_{\mathrm{d}}s}}. \end{aligned} \tag{30}$$

HVA makes i_{c} no longer strictly follow i_{ref} when background harmonics exist in v_{g}. So HVA also stabilizes the APF system in the price of harmonic suppressing precision.

Under the parameters in Table II, bode plots of $T_{\mathrm{pP}}(s)$ when $K_{\mathrm{VA},-11}=0$ and $K_{\mathrm{VA}13}=0.5$, $\sigma_{13}=2\pi*25$ are shown in Fig. 29(a). HVA makes $\angle T_{\mathrm{pP}}(s)$ further from $\pm 180°$, improving the phase margin of $T_{\mathrm{p}}(s)$ as shown in Fig. 29(b). However, after applying HVA, $|T_{\mathrm{p}}(s)|$ is still small around $k\omega_1$. So the improved $T_{\mathrm{p}}(s)$ does not dominate $T(s)$. The oscillating characteristic around -11th harmonic is introduced to $T(s)$ through $T_{\mathrm{p}}^{*}(s^{*}+\mathrm{j}2\omega_1)$ and causes unstable modes, as shown in Fig. 30(a).

So both 13th and -11th HVAs should be applied. Set $\sigma_{-11}=\sigma_{13}=2\pi*25$, $K_{\mathrm{VA},-11}=K_{\mathrm{VA}13}=0.5$ and bode plots are given in Fig. 30(b). HVAs make both $\angle T_{\mathrm{p}}^{*}(s^{*}+\mathrm{j}2\omega_1)$ and $\angle T_{\mathrm{p}}(s)$ not cross $-180°$ around $13\omega_1$, so APF system is effectively stabilized.

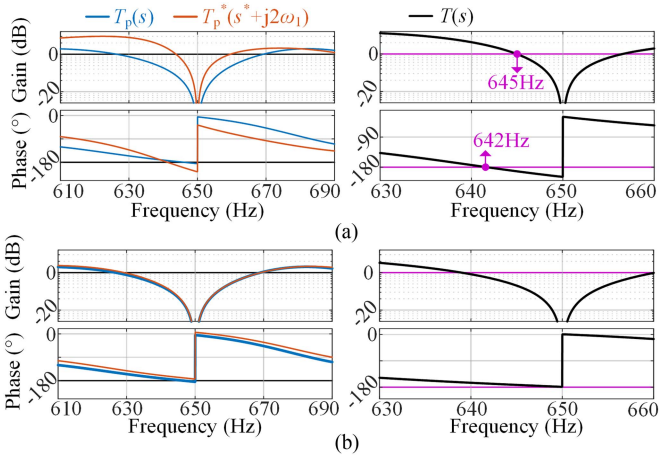

Fig. 30. Bode plots of $T_{\rm p}(s)$, $T_{\rm p}^*(s^*+{\rm j}2\omega_1)$ and $T(s)$ when -11th or 13th HVA is/are applied. (a) Only 13th HVA applied. (b) 13th and -11th HVA applied.

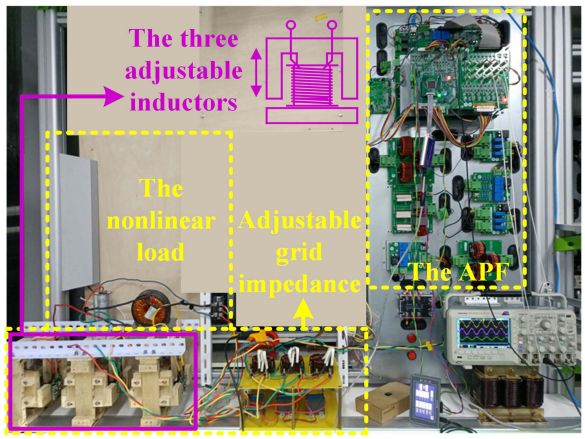

Fig. 31. Bode plots of $T_{\rm p}(s)$, $T_{\rm p}^*(s^*+{\rm j}2\omega_1)$ and $T(s)$ with both -11th and 13th HVA control.

In conclusion, under the frequency coupling effect of the nonlinear load, HVA should be applied to both kth and $(2-k)$th harmonics for effective stabilization.

Therefore, in a situation of low background voltage distortion, HVA should be chosen to stabilize harmonic oscillation for less suppressing precision loss. In the case of high background voltage distortion, HVA causes much remanent harmonics with nonzero $Y({\rm j}k\omega_1)$, so SRR should be chosen because SRR introduces remanence to only one of the kth and $(2-k)$th harmonics.

VI. Verification of Simulations and Experiments

The above analysis indicates the following conclusions.

1) In an APF system, when PRPs get close to the kth ARV, phase deviation, gain bump introduced by PRPs, and phase sharp step introduced by kth ARV will make loop gain $T(s)$ cross $\pm 180°$ where $|T(s)|>1$. Then kth harmonic oscillation happens.
2) Nonlinear load in the APF system causes a frequency coupling effect, making kth and $(2-k)$th harmonics share their resonance dynamics, converging or oscillating together.
3) Frequency coupling promotes the stabilizing effect of SRR method. Reducing $K_{{\rm SR}k}$ can stabilize both kth and $(2-k)$th harmonic oscillation.
4) Frequency coupling degrades the stabilizing effect of the HVA method. HVA should be applied to both kth and $(2-k)$th harmonics to achieve effective stabilization.

To verify these conclusions, simulations and experiments are carried out. The experimental platform includes an APF, a 6-pulse rectifier with resistive load, and a set of grid-side passive components. Equivalent line inductance is realized by three adjustable inductors (as shown at the bottom of Fig. 31), where the inductance depends on an adjustable air gap. The APF's topology is a 3-ph 2-level converter and is controlled by a DSP chip (TMS320F28377D).

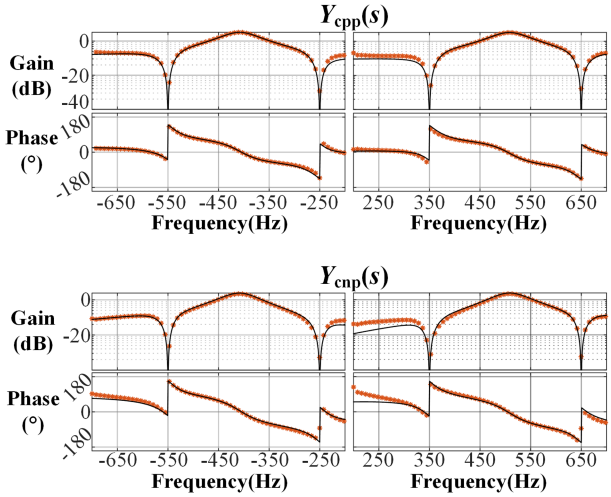

Fig. 32. Comparison between simulation results (in red "*") and theoretical curves (in black line) of $Y_{\rm cpp}(s)$ and $Y_{\rm cnp}(s)$.

A. Accuracy Verifying of the Proposed Models

Models of the APF, 6-pulse rectifier and grid-side impedance $Z_{\rm g}(s)$, are built in this article to analyze the harmonic oscillation. Passive grid-side impedance $Z_{\rm g}(s)$ does not need verifying. So models of the APF and 6-pulse rectifier are verified through frequency-sweeping simulation. Theoretical parallel admittance is easy to extract from Fig. 14, as shown in the following:

$$\begin{bmatrix}\hat{i}_{\rm gp}(s)\\ \hat{i}_{\rm gn}(s)\end{bmatrix}=\begin{bmatrix}Y_{\rm cpp}(s) & Y_{\rm cnp}^*(s^*+{\rm j}2\omega_1)\\ Y_{\rm cnp}(s) & Y_{\rm cpp}^*(s^*+{\rm j}2\omega_1)\end{bmatrix}\begin{bmatrix}\hat{v}_{\rm gp}(s)\\ \hat{v}_{\rm gn}(s)\end{bmatrix}$$

$$\begin{aligned}Y_{\rm cpp}(s)&=-Y(s)+[1-D(s)G_{\rm i}(s)]\,Y_{\rm d}(s-{\rm j}\omega_1)\\ Y_{\rm cnp}(s)&=[1-D(s)G_{\rm i}(s)]\,Y_{\rm d}(s-{\rm j}\omega_1).\end{aligned}\tag{31}$$

A single-frequency voltage perturbation is injected into $v_{\rm g}(f_{\rm p})$. Then positive and negative sequence response $i_{\rm gp}(f_{\rm p})$ and $i_{\rm gn}(2f_1-f_{\rm p})$ are detected to calculate admittance $Y_{\rm cpp}(s)$ and $Y_{\rm cnp}(s)$. Theoretical and simulation results are plotted into one bode plot, as shown in Fig. 32.

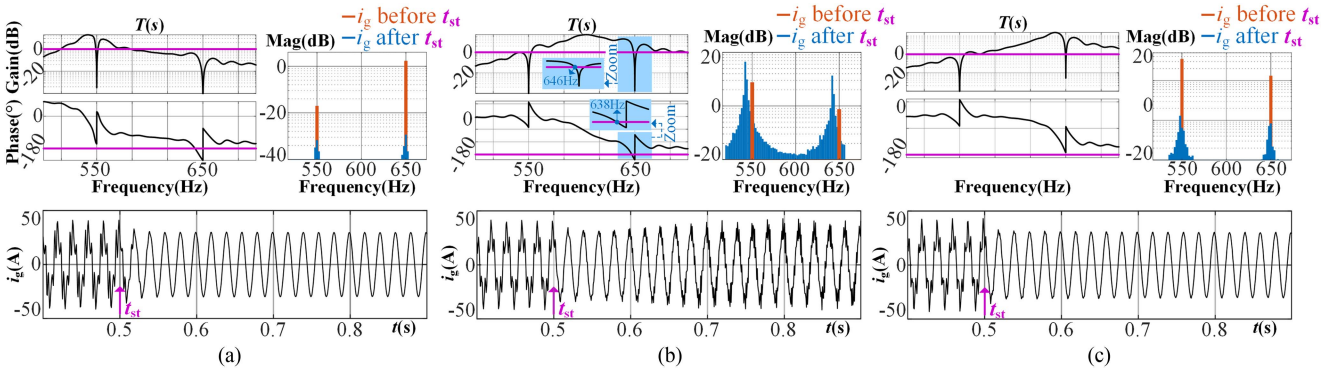

Fig. 33. Simulation verification under different passive resonance frequencies. (a) Low passive resonance frequency. (b) Medium passive resonance frequency. (c) High passive resonance frequency.

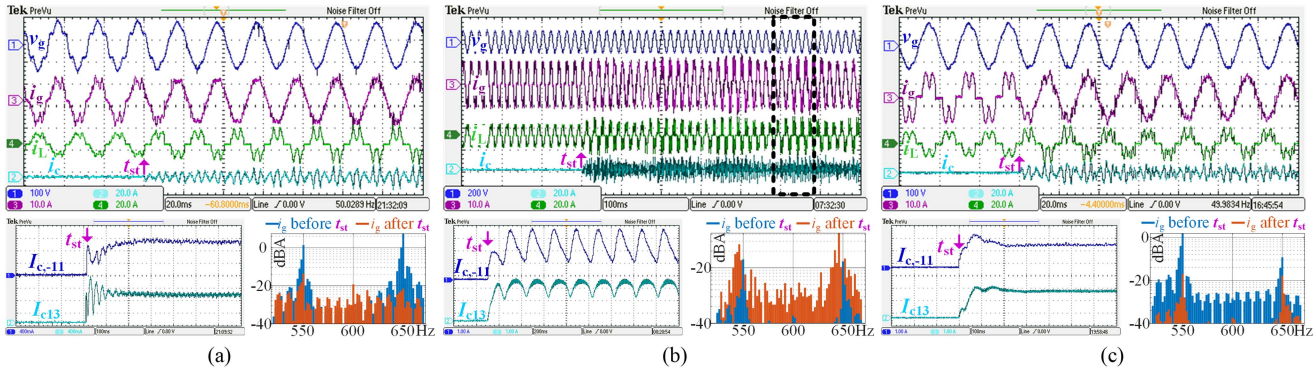

Fig. 34. Experimental verification under different passive resonance frequencies. (a) Low passive resonance frequency. (b) Medium passive resonance frequency. (c) High passive resonance frequency.

Frequency-sweeping results are almost on theoretical curves around harmonic frequencies $(-5\omega_1, 7\omega_1, -11\omega_1, 13\omega_1)$. So the proposed models are precise enough to describe the harmonic resonance characteristic of APF system. Slight deviation on the left of 250 Hz in Fig. 32 is negligible here because it has little influence on the harmonic dynamics.

B. *Verification of Conclusion 1)*

Conclusion 1) shows that the positions of PRPs and ARVs determine harmonic stability. Grid-side equivalent inductor L and filtering inductor $L_{\rm d}$ of 6-pulse rectifier are tuned to make PRPs close to or off from the -11th and 13th ARVs. Simulation results are given in Fig. 33. The APF is turned on at $t_{\rm st}$, and following waveforms show stable or unstable simulation results. Only the positive-frequency half of $T(s)$ is shown because of $T(s)$'s symmetry,. i.e., $T(\mathrm{j}\omega) = T^*(-\mathrm{j}\omega + \mathrm{j}2\omega_1)$.

Fig. 33(b) corresponds to parameters in Table II. Both the frequency-domain theoretical analysis and simulation waveform show unstable results. In Fig. 33(a), L and $L_{\rm d}$ are changed to 1.8 and 3.6 mH for lower PRP frequency. The gain margin appears around $13\omega_1$, so the APF system gets stable. In Fig. 33(c), L and $L_{\rm d}$ are changed to 600 and 800 μH for higher frequency. Phase margin appears, and the APF system also gets stable.

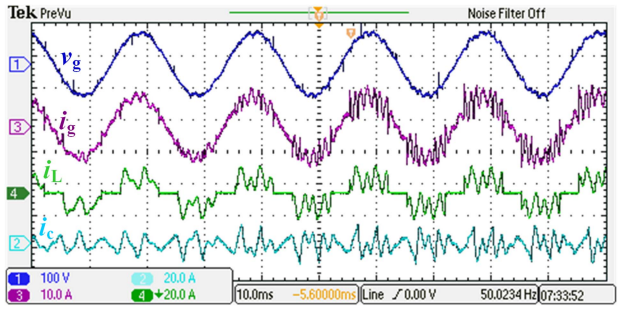

Fig. 35. Zooming in of the ac waveforms in black dashed box of Fig. 34(b).

Experimental results coincide with simulation as shown in Fig. 34. Magnitudes of -11th/13th harmonics in $i_{\rm c}$ are calculated and output from D/A ports, clearly showing the harmonic oscillation. Apparently, in stable conditions [see Fig. 34(a) and (c)], harmonics in $i_{\rm g}$ are effectively suppressed after APF turned ON. Whereas in unstable condition in Fig. 34(b), harmonics are amplified by harmonic oscillation. The zooming in the black dashed box of Fig. 34(b) is shown in Fig. 35.

As shown in Fig. 33(b), frequencies of the oscillating components are close to $-11\omega_1$ and $13\omega_1$, which coincides with the phase crossing point of $T(s)$. This further verifies the precision of the models.

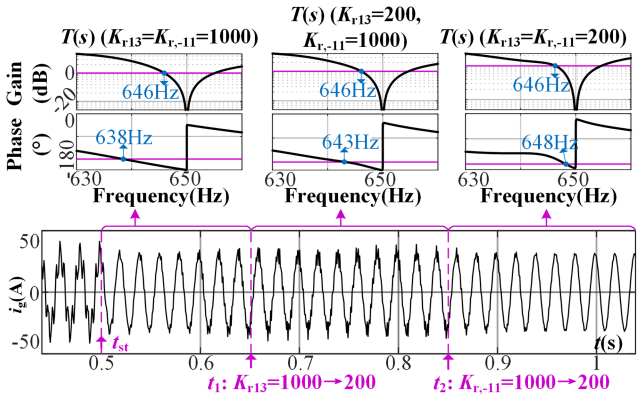

Fig. 36. Simulation with $K_{\mathrm{r}13}$ and $K_{\mathrm{r},-11}$ respectively reduced.

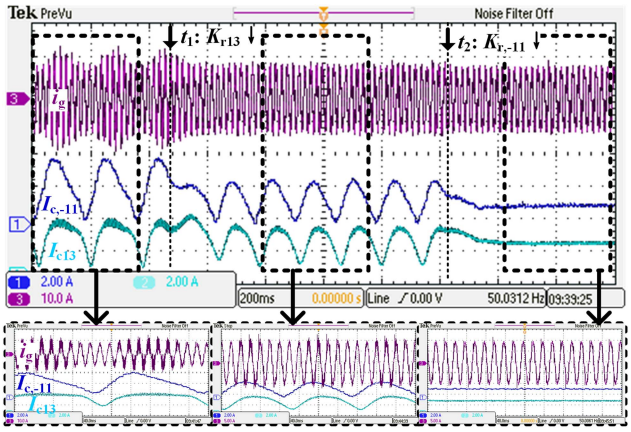

Fig. 37. Experimental waveforms with $K_{\mathrm{r}13}$ and $K_{\mathrm{r},-11}$ respectively reduced

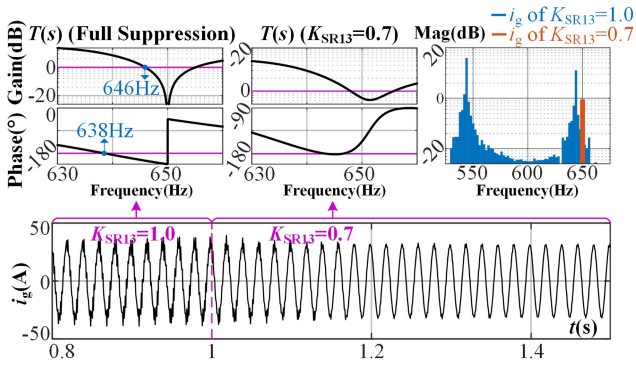

Fig. 38. Simulation of suppression ratio reduction stabilizing method.

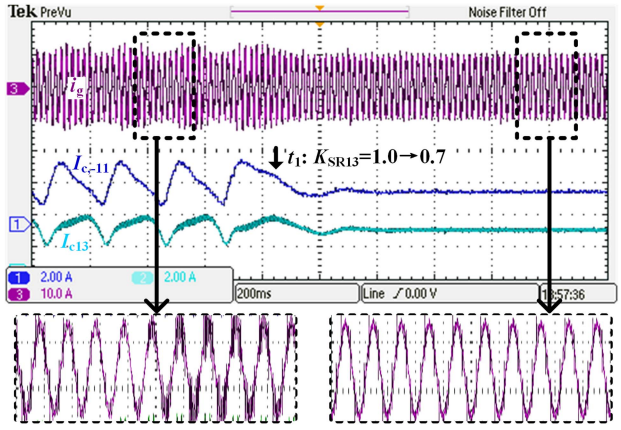

Fig. 39. Experimental waveforms of suppression ratio reduction stabilizing method

C. Verification of Conclusion 2)

Influence of frequency coupling is reflected by adjusting resonator gain K_{rk}, just like analysis in IV-C. In simulation and experiment, key parameters are set according to Table II. Theoretical analysis and simulation waveform of i_{g} are given in Fig. 36. And experimental results are given in Fig. 37.

After the APF being turned ON, the -11th and 13th harmonics oscillate. Then, at t_1 moment, $K_{\mathrm{r}13}$ is reduced from 1000 to 200, which is insufficient for stabilization because of frequency coupling, so $I_{\mathrm{c},-11}$ and $I_{\mathrm{c}13}$ still oscillate. At t_2 moment, $K_{\mathrm{r},-11}$ reduces from 1000 to 200, then both -11th and 13th harmonics converge.

Obviously, reduction of $K_{\mathrm{r},-11}$ and $K_{\mathrm{r}13}$ influences $T(s)$ around both $-11\omega_1$ and $13\omega_1$. So frequency coupling effect introduces strong coupling between the kth and $(2-k)$th harmonics, as conclusion 2) indicates.

D. Verification of Conclusion 3)

To verify the third conclusion, $K_{\mathrm{SR}13}$ (percentage of 13th harmonic suppression) is reduced from 1.0 to 0.7 when the APF system has -11th and 13th harmonic oscillations under the parameters in Table II. Simulation waveforms, spectrums of i_{g}, and corresponding Bode plots are shown in Fig. 38.

Both the waveform and spectrums indicate the effective stabilization introduced by reducing $K_{\mathrm{SR}13}$ from 1.0 to 0.7. Meanwhile, the remanent 13th harmonic appears after reducing $K_{\mathrm{SR}13}$, as the price of stabilization.

Experimental results in Fig. 39 further verify the conclusion. After reducing $K_{\mathrm{SR}13}$ at the moment t_1, harmonic oscillation stops immediately, and i_{g} converges to closely sinusoidal. So effective stabilization on both kth and $(2-k)$th harmonics can be achieved by reducing only $K_{\mathrm{SR}13}$.

E. Verification of Conclusion 4)

To verify conclusion 4), the 13th and -11th HVAs are applied one after another under parameters in Table II. Simulation and experimental results are given in Figs. 40 and 41.

At the moment t_1, 13th HVA is applied with $K_{\mathrm{VA}13}=0.5$ and $\sigma_{13}=2\pi*25$ rad/s. Harmonic oscillations has not been stabilized yet in both simulation and experiment, which coincides with bode plot of $T(s)$ given in Fig. 40. Then, at t_2, -11th HVA joins in. Harmonic oscillations are immediately stabilized in both simulation and experiment.

Therefore, the 13th HVA is not enough to stabilize the 13th harmonic oscillation by itself because the -11th harmonic resonance dynamic also impacts the harmonic stability. For effective stabilization, both 13th and -11th HVA should be applied.

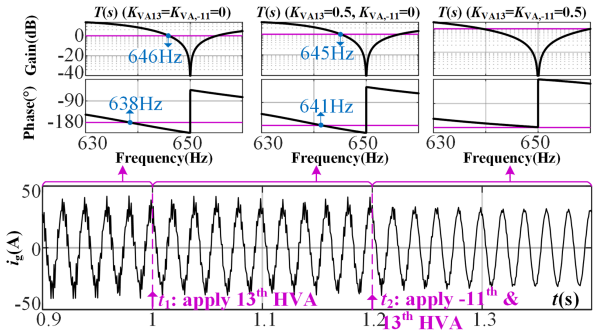

Fig. 40. Simulation with 13th and −11th harmonic virtual admittance control applied one by one.

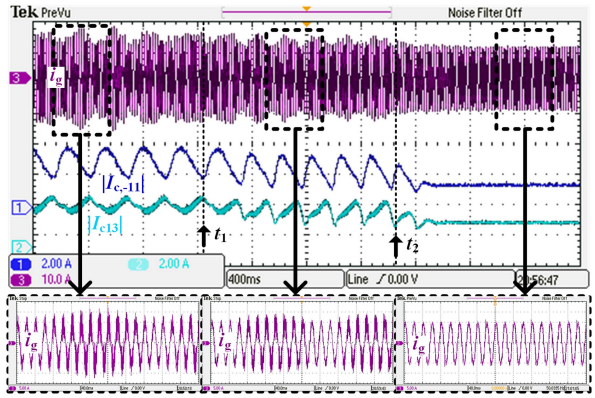

Fig. 41. Experimental waveforms with 13th and −11th harmonic virtual admittance control applied one by one.

VII. Conclusion

This article models a load-current-detected APF system and analyzes the harmonic oscillation issue. Obtained conclusions are listed as follows.

1) The proposed concepts, parallel resonance (reflected by ARVs) and passive resonance (reflected by PRPs) explain harmonic oscillation theoretically. When a PRP gets close to ARV at $k\omega_1$, the APF system will tend to have kth harmonic oscillation.
2) Frequency coupling of the nonlinear load makes the kth and $(2-k)$th harmonics share their resonance characteristics and oscillate together when unstable. The sharing phenomenon cannot be explained with existing theories that ignore the frequency coupling effect.
3) Frequency coupling effect has different influences on SRR and HVA. And the difference can be regarded as guidance when choosing stabilizing strategies under high-distorted or low-distorted grid situations, as explained in Section V-B.

References

[1] X. Meng, M. Chen, M. He, X. Wang, and J. Liu, "Novel high power hybrid rectifier with low cost and high grid current quality for improved efficiency of electrolytic hydrogen production," *IEEE Trans. Power Electron.*, vol. 37, no. 4, pp. 3763–3768, Apr. 2022.

[2] C. Lascu, L. Asiminoaei, I. Boldea, and F. Blaabjerg, "High performance current controller for selective harmonic compensation in active power filters," *IEEE Trans. Power Electron.*, vol. 22, no. 5, pp. 1826–1835, Sep. 2007.

[3] B. S. Chen and G. Joos, "Direct power control of active filters with averaged switching frequency regulation," *IEEE Trans. Power Electron.*, vol. 23, no. 6, pp. 2729–2737, Nov. 2008.

[4] S. Hou, J. Fei, C. Chen, and Y. Chu, "Finite-time adaptive fuzzy-neural-network control of active power filter," *IEEE Trans. Power Electron.*, vol. 34, no. 10, pp. 10298–10313, Oct. 2019.

[5] S. Ouchen, M. Benbouzid, F. Blaabjerg, A. Betka, and H. Steinhart, "Direct power control of shunt active power filter using space vector modulation based on supertwisting sliding mode control," *IEEE Trans. Emerg. Sel. Topics Power Electron.*, vol. 9, no. 3, pp. 3243–3253, Jun. 2021.

[6] D. Yazdani, A. Bakhshai, and P. K. Jain, "Three-phase adaptive notch filter-based approach to harmonic/reactive current extraction and harmonic decomposition," *IEEE Trans. Power Electron.*, vol. 25, no. 4, pp. 914–923, Apr. 2010.

[7] H. Chen, H. Liu, Y. Xing, and H. Hu, "Enhanced DFT-Based controller for selective harmonic compensation in active power filters," *IEEE Trans. Power Electron.*, vol. 34, no. 8, pp. 8017–8030, Aug. 2019.

[8] H. Yi et al., "Source-current-Detected shunt active power filter control scheme based on vector resonant controller," *IEEE Trans. Ind. Appl.*, vol. 50, no. 3, pp. 1953–1965, May/Jun. 2014.

[9] X. Sun, J. Zeng, and Z. Chen, "Site selection strategy of single-frequency tuned R-APF for background harmonic voltage damping in power systems," *IEEE Trans. Power Electron.*, vol. 28, no. 1, pp. 135–143, Jan. 2013.

[10] A. Luo, S. Peng, C. Wu, J. Wu, and Z. Shuai, "Power electronic hybrid system for load balancing compensation and frequency-selective harmonic suppression," *IEEE Trans. Ind. Electron.*, vol. 59, no. 2, pp. 723–732, Feb. 2012.

[11] H. Yuan and X. Jiang, ""simple active damping method for active power filters," in *Proc. IEEE Appl. Power Electron. Conf. Expo.*, 2016, pp. 907–912.

[12] L. Yang, J. Yang, M. Gao, A. Watson, and P. Wheeler, "Current control of LCL-Type shunt APFs: Damping characteristics, stability analysis, and robust design against grid impedance variation," *IEEE Trans. Emerg. Sel. Topics Power Electron.*, vol. 9, no. 4, pp. 5026–5042, Aug. 2021.

[13] P. Dang, T. Ellinger, and J. Petzoldt, "Dynamic interaction analysis of APF systems," *IEEE Trans. Ind. Electron.*, vol. 61, no. 9, pp. 4467–4473, Sep. 2014.

[14] J. Lei, Z. Qin, W. Li, P. Bauer, and X. He, "Stability region exploring of shunt active power filters based on output admittance modeling," *IEEE Trans. Ind. Electron.*, vol. 68, no. 12, pp. 11696–11706, Dec. 2021.

[15] L. Harnefors, A. G. Yepes, A. Vidal, and D.-J. Gandoy, "Passivity-based controller design of grid-connected VSCs for prevention of electrical resonance instability," *IEEE Trans. Ind. Electron.*, vol. 62, no. 2, pp. 702–710, Feb. 2015.

[16] Q. Geng, H. Sun, X. Zhang, X. Zhou, J. Liang, and Y. Geng, "Mitigation of oscillations in three phase LCL-filtered grid converters based on proportional resonance and improved model predictive control," *IEEE Trans. Ind. Appl.*, vol. 59, no. 2, pp. 2590–2602, Mar./Apr. 2023.

[17] C. Chen, J. Xiong, Z. Wan, J. Lei, and K. Zhang, "Time delay compensation method based on area equivalence for active damping of an LCL-type converter," *IEEE Trans. Power Electron.*, vol. 32, no. 1, pp. 762–772, Jan. 2017.

[18] Y. He, X. Wang, X. Ruan, D. Pan, and K. Qin, "Hybrid active damping combining capacitor current feedback and point of common coupling voltage feedforward for LCL-Type grid-connected inverter," *IEEE Trans. Power Electron.*, vol. 36, no. 2, pp. 2373–2383, Feb. 2021.

[19] X. Li, X. Wu, Y. Geng, X. Yuan, C. Xia, and X. Zhang, "Wide damping region for LCL-Type grid-connected inverter with an improved capacitor-current-feedback method," *IEEE Trans. Power Electron.*, vol. 30, no. 9, pp. 5247–5259, Sep. 2015.

[20] Y. Zhang, K. Dai, X. Chen, Y. Kang, and Z. Dai, "An improved method of SAPF for harmonic compensation and resonance damping with current detection of power capacitors and linear/nonlinear loads," in *Proc. IEEE Appl. Power Electron. Conf. Expo.*, 2017, pp. 3286–3291.

[21] Y. Zhang, K. Dai, X. Chen, Y. Kang, and Z. Dai, "Stability analysis of SAPF by viewing DFT as cluster of BPF for selective harmonic suppression and resonance damping," *IEEE Trans. Ind. Appl.*, vol. 55, no. 2, pp. 1598–1607, Mar./Apr. 2019.

[22] K. Liu et al., "Admittance modeling, analysis, and reshaping of harmonic control loop for multiparalleled SAPFs system," *IEEE Trans. Ind. Inform.*, vol. 17, no. 1, pp. 280–289, Jan. 2021.

[23] W. Pan, D. Li, and X. Yang, "Analysis and suppression of harmonic oscillation caused by active power filter with magnetic flux compensation," in *Proc. IEEE 3rd Int. Conf. Electron. Technol., Commun. Inf.*, 2023, pp. 531–536.
[24] S. Jian, B. Zhonghui, and K. J. Karimi, "Input impedance modeling of multipulse rectifiers by harmonic linearization," *IEEE Trans. Power Electron.*, vol. 24, no. 12, pp. 2812–2820, Dec. 2009.
[25] L. Yu, L. Xu, J. Zhu, and R. Li, "Impedance modelling and stability analysis of diode-rectifier based HVDC connected offshore wind farms," *IEEE Trans. Power Del.*, vol. 37, no. 1, pp. 591–602, Feb. 2022.
[26] X. Yue, X. Wang, F. Blaabjerg, D. Boroyevich, R. Burgos, and F. Lee, "Wideband small-signal input dq admittance modeling of six-pulse diode rectifiers," in *Proc. IEEE Appl. Power Electron. Conf. Expo.*, 2018, pp. 1981–1988.
[27] M. Jaksic et al., "Nonlinear sideband effects in small-signal input dq admittance of six-pulse diode rectifiers," in *Proc. 28th Annu. IEEE Appl. Power Electron. Conf. Expo.*, 2013, pp. 2761–2768.
[28] H. Nian, L. Chen, Y. Xu, H. Huang, and J. Ma, "Sequences domain impedance modeling of three-phase grid-connected converter using harmonic transfer matrices," *IEEE Trans. Energy Convers.*, vol. 33, no. 2, pp. 627–638, Jun. 2018.
[29] S. Shah and L. Parsa, "Impedance modeling of three-phase voltage source converters in DQ, sequence, and phasor domains," *IEEE Trans. Energy Convers.*, vol. 32, no. 3, pp. 1139–1150, Sep. 2017.
[30] X. Wang, L. Harnefors, and F. Blaabjerg, "Unified impedance model of grid-connected voltage-source converters," *IEEE Trans. Power Electron.*, vol. 33, no. 2, pp. 1775–1787, Feb. 2018.
[31] W. Wu et al., "Sequence-impedance-based stability comparison between VSGs and traditional grid-connected inverters," *IEEE Trans. Power Electron.*, vol. 34, no. 1, pp. 46–52, Jan. 2019.
[32] L. Harnefors, "Modeling of three-phase dynamic systems using complex transfer functions and transfer matrices," *IEEE Trans. Ind. Electron.*, vol. 54, no. 4, pp. 2239–2248, Aug. 2007.
[33] N. M. Wereley, "Analysis and control of linear periodically time varying systems," Ph.D. dissertation, Massachusetts Inst. Technol., Dept. Aeronaut. Astronaut., 1991.
[34] L. Fan and Z. Miao, "Admittance-based stability analysis: Bode plots, nyquist diagrams or eigenvalue analysis?," *IEEE Trans. Power Syst.*, vol. 35, no. 4, pp. 3312–3315, Jul. 2020.
[35] Z. Hao, J. Gong, Y. Liu, S. Pan, and X. Zha, "Analytical calculation of the DC-Link current harmonics in active power filter considering coupling effect," *IEEE J. Emerg. Sel. Topics Ind. Electron.*, vol. 4, no. 3, pp. 767–780, Jul. 2023.

Yuguo Li (Student Member, IEEE) was born in Sichuan, China, in 1996. He received the B.S. degree in electrical engineering, in 2018, from Xi'an Jiaotong University, Xi'an, China, where he is currently working toward the Ph.D. degree in stability analyzing of grid-connected converters with the Department of Electrical Engineering.

His research interests include power quality and control of power electronic converters.

Hao Yi (Member, IEEE) received the Ph.D. degree in electrical engineering from Xi'an Jiaotong University (XJTU), Xi'an, China, in 2013.

He visited the Department of Energy Technology, Aalborg University, Aalborg, Denmark, from 2016 to 2017. He is currently an Associate Professor with XJTU. In the fields of his research interests, he hosted one prize and published more than 70 articles. His research interests include power electronics technologies used in power quality control, distributed power control, and grid-connected converter modeling/control.

Fang Zhuo (Member, IEEE) was born in Shanghai, China, in 1962. He received the B.S. degree in automatic control and the M.S. and Ph.D. degrees in automation and electrical engineering from Xi'an Jiaotong University (XJTU), Xi'an, China, in 1984, 1989, and 2001, respectively.

He was an Associate Professor with XJTU in 1996, where he became a Full Professor of Power Electronics and Drives in 2004. He was a supervisor of Ph.D. students. He is the key finisher of the four projects sponsored by the National Natural Science Foundation of China and more than 40 projects cooperated with companies from the industry. He holds four patents. His research interests include power electronics, power quality, active power filter, reactive power compensation, and inverters for distributed power generation.

Dr. Zhuo is a Member of the China Electro Technical Society, the Automation Society, and the Power Supply Society. He received four provincial- and ministerial-level science and technology advancement awards. He is also the Power Quality Professional Chairman of the Power Supply Society in China.

Xin Jiang (Graduate Student Member, IEEE) was born in Sichuan, China, in 1998. He received the B.S. degree in electrical engineering from Sichuan University, Chengdu, China, in 2020. He is currently working toward the Ph.D. degree in modelling and controlling of DC-AC converters with the Department of Electrical Engineering, Xi'an Jiaotong University, Xi'an, China.

His research interests include small signal stability and control of power electronic converters.